

Nanoparticles and Clusters

Chapter Outline

10.1. Introduction	408	10.2.8. Modeling Heterogeneous Nanoparticles	420
10.2. Information in the PDFs of Nanoparticles	408	10.2.9. Surface Capping Ligand Dependence of Nanoparticle Structure	422
10.2.1. Nanoparticle Size and Shape	411		
10.2.2. Nanoparticle Structure and Defects	412		
10.2.3. <i>Ab Initio</i> Solution of Unknown Nanostructures	416	10.3. Clusters Suspended in a Solvent	423
10.2.4. Homogeneous Size-Dependent Strain in Nanoparticles	416	10.3.1. Precursors to Gold Nanoparticle Formation	424
10.2.5. Nanoparticle Thermodynamic Quantities from the PDF	417	10.3.2. Time-Resolved Studies of Hydrothermal Chemical Reactions	426
10.2.6. Surface to Volume Ratio and Inhomogeneous Strains in Nanoparticles	418	10.3.3. Structures of Surfactant Micelles Suspended in Water	428
10.2.7. Size-Dependent Bond Stiffness in Nanoparticles	419	10.3.4. Structure of Pt(II) ion Complexes in Water	430
		10.4. Clusters and Molecules Intercalated in Nanoporous Solids	431

10.4.1. Hydrogen in a Cyanide Host	431	10.4.3. Mercury in Silica	434
10.4.2. Metal Organic Frameworks and ZIFs	432	10.4.4. Sodium in Silica	434

10.1. INTRODUCTION

One of the largest growing areas for application of PDF methods to materials science since the first edition of this book has been in the area of nanoparticles and clusters. A number of factors are combining to make this an important area of study. First, as we have described at length, PDF methods are becoming more powerful with the advent of new, more intense sources, new methods such as rapid acquisition pair distribution function (RAPDF) and Electron PDF (ePDF) and dedicated beamlines for carrying out measurements with these methods. Second, computational power is also growing at a similar rate, as are the sophistication of the software tools for analyzing and modeling the data. The third leg is that nanoparticle (NP) research itself is exploding, with new methods for making nanoparticles with even more precise control of composition, shape, and size, and with many application areas being explored from medical fluorescence labeling, through targeted drug delivery, and catalysis to efficient photovoltaics and ambient lighting light emitting diode lamps. Finally, there appears to be a very good match between modern PDF methods and nanoparticle research. In this domain, it is very difficult to do crystallography because of the broad and somewhat featureless diffraction patterns, but unlike in glasses and liquids, there is still sufficient information in the PDF to allow rather sophisticated modeling to be carried out. In addition to nanoparticles, the PDF can be applied to the “Babinet couple” to the nanoparticle, which is the nanoporous material.

There are a large numbers of PDF studies (for some early examples not described below, see [Zhang et al., 2003](#); [Gilbert et al., 2004a,b](#); [Page et al., 2004](#); [Petkov et al., 2005](#); [Petkov et al., 2006](#); [Knecht et al., 2008](#)) on nanoparticles that are emerging, and this chapter is not an exhaustive review on the subject, but should give some flavor of what kind of information can be obtained from the PDF, and how it is done.

10.2. INFORMATION IN THE PDFS OF NANOPARTICLES

We use the example of CdSe nanoparticles ([Masadeh et al., 2007](#)) to illustrate the kind of information and its precision that can be obtained from nanoparticle samples. These are the archetypal quantum dot nanoparticles that essentially gave birth to the modern field, when it was discovered how to make them using arrested precipitation from solvent ([Bawendi et al., 1989](#)). They have many applications due to their optoelectronic properties ([Colvin et al.,](#)

1994; Tolbert and Alivisatos, 1994; Murray *et al.*, 1995; Bruchez *et al.*, 1998; Li and Alivisatos, 2003). They resemble structurally their bulk II–VI semiconducting cousins, where the cations and anions form a network of tetrahedra similar to the diamond structure such that both the group II and group VI ions are both tetrahedrally coordinated by the other species. It is a fully 3D structure, but the tetrahedra can be thought of as forming layers that stack, and depending on the stacking arrangement, the bulk crystal structure is either cubic (zinc blende) or rhombohedral (wurtzite). In the former case, the stacking has an ABCABC motif, and in the latter, it is ABABABA, similar to the case for closely packed structures that give rise to face centered cubic and hexagonal close packed structures. However, it is difficult to study the structure in detail. The reason is that the small size of the nanoparticles causes the diffraction patterns to broaden out due to finite size effects. This is illustrated in Fig. 10.1 which shows 2D diffraction patterns collected on an image-plate detector using X-rays from the Advanced Photon Source (Masadeh *et al.*, 2007). On the left is the diffraction pattern from the bulk material, and on the right is that from CdSe nanoparticles of roughly 4 nm diameter. Clearly defined sharp diffraction lines are evident as circles in the left panel. These are broadened out into diffuse rings in the nanoparticle diffraction pattern. This can also be seen in the 1D diffraction patterns shown in Fig. 10.2. This broadening and loss of structural information due to the small size of the nanoparticles makes them very difficult to study using traditional powder diffraction methods as was pointed out early on (Bawendi *et al.*, 1989). Actually, the early paper by Bawendi *et al.* (1989) is a tour de force of structural analysis given the tools and methods of the time. However, modern total scattering approaches outlined in this book result in a wealth of precise and quantitative information.

The nanoparticles used in this study were designated III, II, and I, and they are roughly 4, 3, and 2 nm diameter, respectively. The experiments were made possible with the advent of the RAPDF data acquisition method described in Chapter 4. Earlier attempts to measure PDFs over a wide range

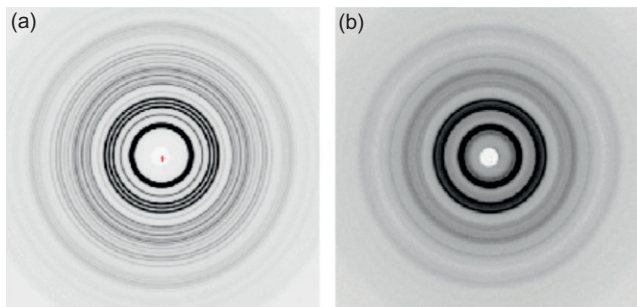


FIGURE 10.1 Comparison of the 2D diffraction patterns from (a) bulk and (b) nanocrystalline CdSe. Note that the bulk sample has sharp, well-resolved rings whereas these are broadened out in the nanoparticle diffraction pattern (Masadeh *et al.*, 2007).

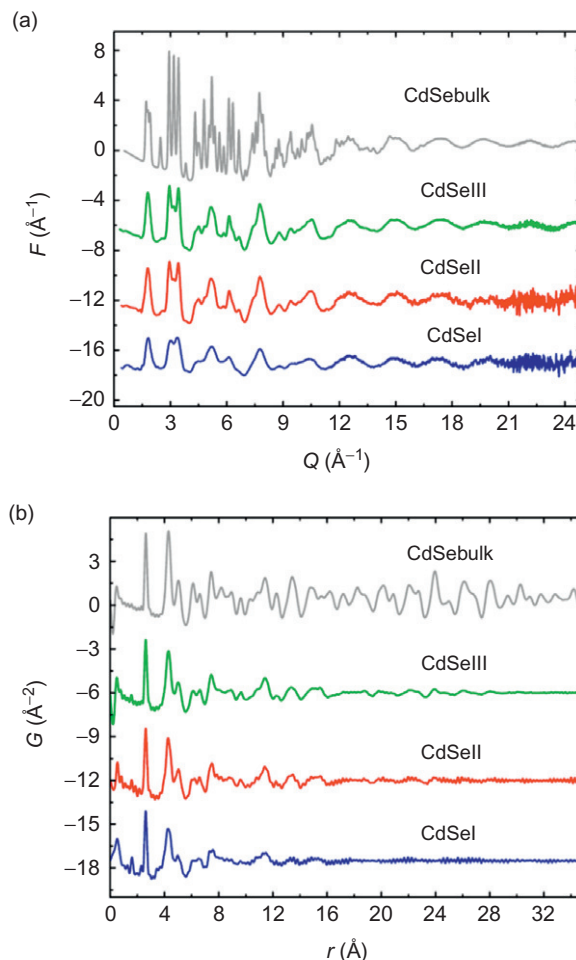


FIGURE 10.2 (a) The $F(Q)$ functions from the bulk and nanocrystalline CdSe nanoparticles. CdSe III, II, and I are around 4, 3, and 2 nm diameter nanoparticles. (b) The PDFs obtained from the data in (a) ([Masadeh et al., 2007](#)).

of Q resulted in beam damage to the sample as it was exposed to an intense synchrotron beam for many hours. In fact, at the end of the experiment, a small hole was found in the sample, ringed by brown burned material, at the position of the beam. The instability of the sample is related to the small size of the particles, and the organic surfactant capping that is used to stabilize them at this small size. The surfactant was literally cooked by the beam. In the subsequent RAPDF measurements, the samples were exposed to the beam for only a few minutes, and subsequent detected frames were compared to ensure that the signal was time stable.

10.2.1. Nanoparticle Size and Shape

A close examination of Fig. 10.2 indicates, as expected, that features in the diffraction patterns broaden with decreasing nanoparticle size. Because the data were measured over such a wide range of Q -space, it is possible to see extensive diffuse scattering that is quite reproducible between the datasets. This will result in crucial information in the PDFs which are shown in panel (b). What is apparent in the PDFs is that, at low- r , the features in all the PDFs are quite similar for all the samples. Further, the features are comparably sharp in the low- r region. There is no (or very little as we discuss later) broadening of the PDF features due to the finite size of the nanoparticles. On the other hand, the features evident in the bulk sample at high- r diminish and disappear with increasing r in the nanoparticle samples. This is because of the small size of the nanoparticles. In a spherical nanoparticle, there can be no atom-pairs that exceed the diameter of the particle, d , and so the PDF clearly has to diminish to zero at $r=d$. The functional form of this falloff depends on the shape of the nanoparticle, as discussed in Chapter 3. It tends to fall off smoothly, as a power law, because as the interatomic vector gets longer, there are fewer and fewer pairs of atoms that can be found in the sample with that separation. For nearest neighbor peaks, there are many pairs present in the bulk and all the way to the surface of the nanoparticle. By the time you reach $r=d$, the only atoms that can possibly be separated by this distance lie on the surface of the nanoparticle (and are separated by the diagonal). In this way, features in the PDF at different distances contain subtly different information about bonding in different parts of the nanoparticle. This level of information has only begun to be extracted through modeling.

The nanoparticles in this study were roughly spherical and could fit well with a spherical characteristic function. The characteristic functions are the same as those used in the small angle scattering (SAS) literature (Farrow and Billinge, 2009), and many of the derivations go back a long time (e.g., see Guinier *et al.*, 1955). A useful recent treatment specific for PDF studies is given in Kodama *et al.* (2006). For spherical nanoparticles, there is just one fitting parameter, the diameter. Care should be taken when interpreting nanoparticle sizes from different techniques. The “size” of the nanoparticle obtained from the PDF is a measurement of the size of the coherently scattering structural domain, averaged over all the nanoparticles that are probed by the beam. If the nanoparticles are structurally well ordered as they were in this case, this is also the size of the nanoparticle. In other cases, such as the ZnS studied by Zhang *et al.* (2003), the coherent structural core is smaller than the physical size of the nanoparticle. People talk about a “surface amorphous” region, though the reality of the situation is likely to be more subtle and interesting, and we are only starting to understand how nanoparticles relax structurally in reality. In any case, the PDF measurement of “size” places a robust lower-bound on the nanoparticle size, which may actually be larger.

On the other hand, SAS is insensitive to the internal structure of the nanoparticles but is sensitive to the scattering density. If we assume any “surface amorphous” region has a similar density to the crystalline core, then the SAS measurement actually measures the physical size of the nanoparticle. SAS and PDF data are therefore highly complementary for nanoparticle studies and increasingly will be combined in the future, as we discussed in [Chapter 3](#). TEM data are somewhat in-between. First, nanoparticle size determined from TEM is not a full sample average. Normally, as many nanoparticles as possible are measured from images taken in different regions of the sample at moderate resolution, and a particle size distribution is determined. This is somewhat arduous and human-intensive process, and the number of the samples studied is proportional to the patience of the graduate student doing the analysis. The edge of the nanoparticle is also often indistinct, and there may be some systematic underestimation of particle size if the thin edges of the particles are not clearly seen. If the surfaces of the nanoparticles are more disordered, they will also diffract less strongly than the core region and appear lighter which produces another bias toward underestimating nanoparticle size from TEM images. However, absolutely crucial information coming from the TEM sizes estimations that is not easily determined from the heavily averaged SAS and PDF data are the particle size distributions (i.e., the range of nanoparticle sizes in the sample) and the shapes of the samples. This information is in the PDF and SAS data in principle but is hard to extract definitively. For example, we have found that similar fits can be obtained to PDFs from nanoparticles using both a model of spherical particles with a modest Gaussian distribution of nanoparticle sizes and a model of spheroid-shaped nanoparticles. Complementary TEM information can distinguish these cases rather easily, and this information is used to constrain the PDF modeling. There is no systematic study that we know of between nanoparticle sizes from PDF and other common measures of size obtained from, for example, the photoabsorption or photoluminescent spectra from the nanoparticles. In the current CdSe study, the sizes obtained from those measurements agreed well with the size from the PDF measurement ([Masadeh *et al.*, 2007](#)).

10.2.2. Nanoparticle Structure and Defects

In addition to the information about the particle size, the PDF contains information about the internal atomic structure of the nanoparticles. In the case of CdSe, the nanoparticles could have the wurtzite or the zinc blende structure. This can be probed by modeling the PDF. [Figure 10.3](#) shows the results of those fits. For the bulk, the wurtzite model is clearly preferred. However, for the different nanoparticles, each model seems to give a comparable fit to the data, as evidenced by the difference curves offset below the PDFs of the data and the best-fit models. The fits are reasonably good, so the structure in these nanoparticles is clearly the tetrahedral bonding motif of the bulk, but it is hard to

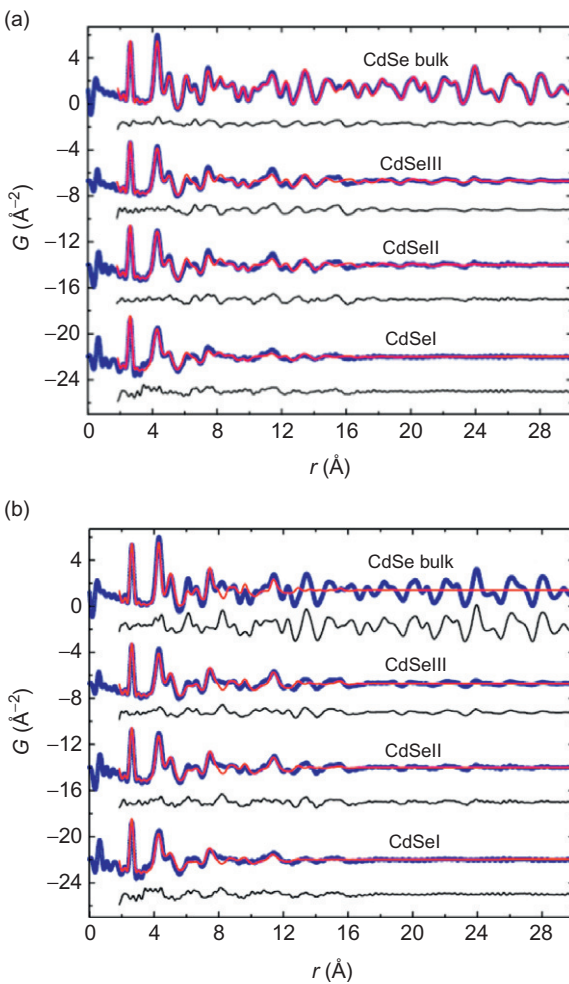


FIGURE 10.3 Comparison of model fits to the PDFs. (a) The solid lines are fits of the wurtzite model to the data shown as symbols. Offset below are difference curves. (b) As (a), except these are the zinc blende structural model fits (Masadeh *et al.*, 2007).

unambiguously say whether the structure is zinc blende or wurtzite. Actually, what turns out to be the case is that the nanoparticles have significant stacking fault defects. As we discussed above, the difference between wurtzite and zinc blende is ABABAB versus ABCABC stacking, respectively stacking along the rhombohedral z -direction (the cubic [1 1 1] direction). This was discovered in the first place by the observation of an overly large atomic displacement parameter (ADP) along the wurtzite z -direction (U_{33}) in fits where anisotropic ADPs were refined. This is reminiscent of fits to layered materials that have

turbostratic disorder (the layers do not line up in an ordered way), such as disordered graphite ([Petkov et al., 1999](#)). There are sharp interatomic correlations between atoms within a layer, but broad (or essentially nonexistent) PDF peaks between pairs of atoms in adjacent layers. The modeling software compensates for that by putting an insanely large and nonphysical ADP in the stacking direction. The resulting cigar shaped atomic density distributions result in a PDF that mimics that from one with well defined interlayer order but no interlayer order by smearing the interlayer correlations. They are not physically meaningful but indicative of the stacking disorder. To check this result in the case of CdSe, a number of models were created with explicit stacking fault densities in them and their PDFs calculated. This was done using the DISCUS modeling program ([Neder and Proffen, 2009](#)). It is a somewhat arduous process because the correct PDF should be an average over many configurations of different faulted NPs stochastically created with a given stacking fault density. This process is accurate but somewhat slow. The resulting PDFs were then fit using the wurtzite models with the U_{33} parameter refined. Using this approach, stacking fault densities close to 50% were detected, meaning that the next layer after an AB stacking will be A with 50% probability and C with 50% probability, that is, the stacking is random. This will not be true for all nanoparticles but was the observation in this case. This explains why the wurtzite and zinc blend models gave comparably good (or comparably bad) fits to the nanoparticle data in [Fig. 10.3](#). Their actual structure is almost exactly halfway between wurtzite and zinc blend, so neither model was preferred. Models with stacking faults on the other hand gave much better fits. It is worth remembering in these discussions that the nanoparticles in question do not have many atomic layers in them in which to accommodate a stacking fault defect. The layers are separated by around 3.5 Å or 0.35 nm, so there are roughly eight layers in a 3-nm diameter particle and six in a 2-nm diameter particle. It takes four layers to define a stacking fault, that is, ABAC or ABCB, so in any given nanoparticle, there is likely to be only a very small number, for example, 1 or 2, of stacking faults.

RuO_2 is an excellent electron conductor and is used in electronic devices. When it is hydrated and made into nanoparticles, the mixture is a good conductor for electrons and protons. It is thus a promising material for supercapacitor or fuel cells. A strongly hydrated nanoparticles show very broad diffraction peaks and were judged to be amorphous by diffraction and EXAFS studies ([McKeown et al., 1999](#)). However, an X-ray PDF study demonstrated that the local structure remains crystalline down to 0.5 nm in size, as shown in [Fig. 10.4](#). This explains why the mixture retained good electronic conductivity in spite of strong disorder, because amorphous RuO_2 would not be metallic ([Dmowski et al., 2002](#)). On the other hand, the structure can become different from the bulk in nanoparticles. Gold is inert in bulk but can be catalytically active as nanoparticles ([Haruta, 1997](#)). An X-ray PDF study of gold nanoparticles in silica showed that the local structure of gold become distorted as temperature is slightly raised, as shown in [Fig. 10.5](#) ([Dmowski et al., 2010](#)). Such

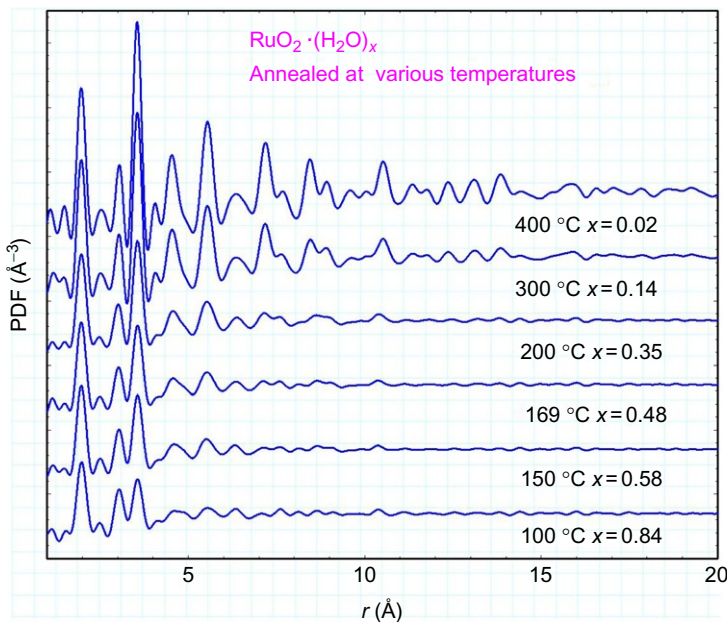


FIGURE 10.4 X-ray PDF of hydrated ruthenia, $\text{RuO}_2 \cdot (\text{H}_2\text{O})_x$ (Dmowski *et al.*, 2002). Temperature indicates annealing temperature. At higher annealing temperatures, more water is lost and nanoparticles grow in size.

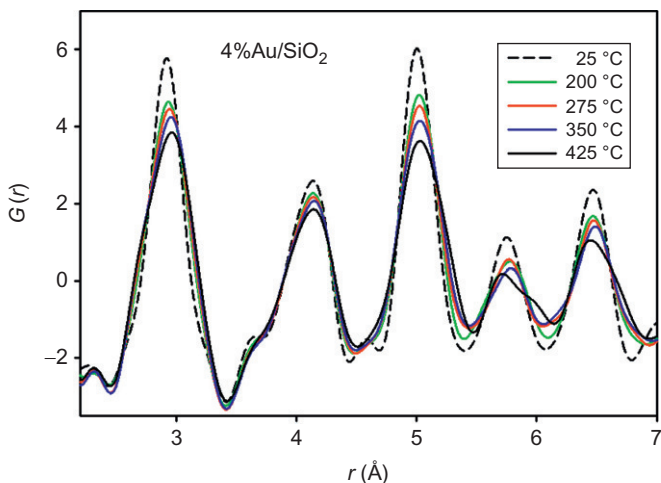


FIGURE 10.5 X-ray PDF of nanoparticle gold in silica (Dmowski *et al.*, 2010). As temperature is increased, the first peak splits into two subpeaks, even though the average structure remains f.c.c., suggesting local shear distortion of gold atomic environment.

distortion would bring the top of the *d*-electron band closer to the Fermi-level, and make it active for catalytic reaction.

10.2.3. *Ab Initio* Solution of Unknown Nanostructures

In the discussion to date, the structure of the nanoparticles resembled that of the bulk materials. As we discuss below, when the nanoparticles get to be very small, their structure modifies and is no longer that of a small piece of bulk material. In this case, we need approaches to solve the structure of small nanoparticles. As we mentioned in [Chapter 6](#), some progress has been made on *ab initio* structure solution from PDF data ([Juhas et al., 2006, 2008](#)). Progress is also being made on structure solution using near atomic resolution 3D tomography or diffraction imaging of individual nanoparticles in the TEM or in a hard X-ray free electron laser ([Zuo et al., 2003; Chapman et al., 2011; Seibert et al., 2011; Scott et al., 2012](#)). These methods are developing rapidly but are still quite immature. In the mean time, it is necessary to use trial and error methods to determine unknown nanoparticle structures, which is quite problematic.

10.2.4. Homogeneous Size-Dependent Strain in Nanoparticles

In addition to the structural model, structural defects, and size, the PDF also contains accurate information about strains in the nanoparticle. In bulk materials, the strain is a continuum property that is expressed in terms of a fractional change in some parameter such as the lattice parameter. It may be directional and is then measured by changes in average separations of particular lattice planes. It is not so clear how to define strain in a small object such as a nanoparticle. However, a change in the average lattice parameter of a crystal really comes down to a change in bond lengths within the material, and bond lengths can be measured reliably using the PDF. We can thus define a bond strain as $\Delta r_{ij}/r_{ij}$, where r_{ij} is the bond length between atom *i* and atom *j* and Δr_{ij} is a change in the bond length. The change in bond length may be produced by applying a stress, but it could also come from a change in temperature (in which case it is the thermal expansion), or for the case of nanoparticles, due to a change in the size of the nanoparticle. The effect on the Cd—Se bond length of decreasing the NP size is shown in [Fig. 10.6](#). The position of the peak clearly shifts to the left for decreasing nanoparticle diameter indicating a size-dependent compressive strain. Defining $\Delta r_{ij} = r_{ij}(d) - r_{ij}(\infty)$, where $r_{ij}(d)$ is the bond length for a nanoparticle of diameter *d*, we can plot the strain versus nanoparticle size. The PDF clearly measures this accurately enough to be able to detect a strain of 0.1%. As is evident in [Fig. 10.6](#) ([Masadeh et al., 2005](#)), the compressive strain increases in amplitude with decreasing NP size. Similar experiments on even smaller nanoparticles show that the curve continues downward to a more compressive strain as the NP diameter decreases further. Observation of size-dependent strains in

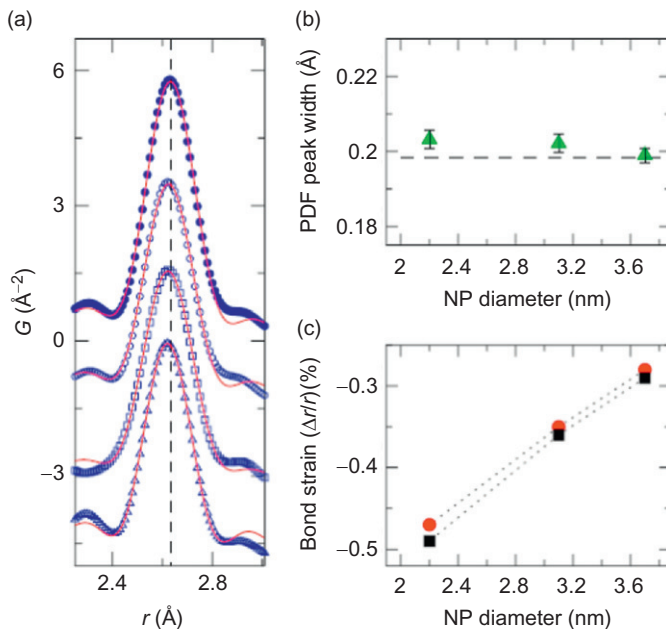


FIGURE 10.6 (a) Plot of the first neighbor Cd—Se peak in the PDFs. Symbols are the PDF data and the solid line is a fit to the curve. From top to bottom: bulk, 4, 3, and 2 nm diameter nanoparticles. Measured (b) inhomogeneous and (c) homogeneous strain plotted versus nanoparticle size (Masadeh *et al.*, 2007).

nanoparticles is now quite ubiquitous. It may be due to a surface stress, which increases with decreasing NP size because of the increasing surface to volume ratio. However, some nanoparticles, notably oxides, show the opposite behavior and expand with decreasing diameter. The physics of nanoparticles is only beginning to be understood.

10.2.5. Nanoparticle Thermodynamic Quantities from the PDF

The PDF may also be used to extract thermodynamic quantities for nanoparticles that are difficult to extract otherwise. In a similar study (Redmond *et al.*, 2012), the size-dependent strain in Pt nanoparticles used as catalysts in, for example, fuel cell electrodes was used to determine the surface energy of the small nanoparticles. Surface energy is a continuum thermodynamic quantity with an atomic origin. It is not clear when the curvature of the surface is as great as it is in nanoparticles that it makes sense to define such a quantity. Nonetheless, it is possible to do so and knowing this quantity is useful. But how to measure it? If we assume that the bond contraction in this material is due to an effective surface stress (which is related to the surface energy),

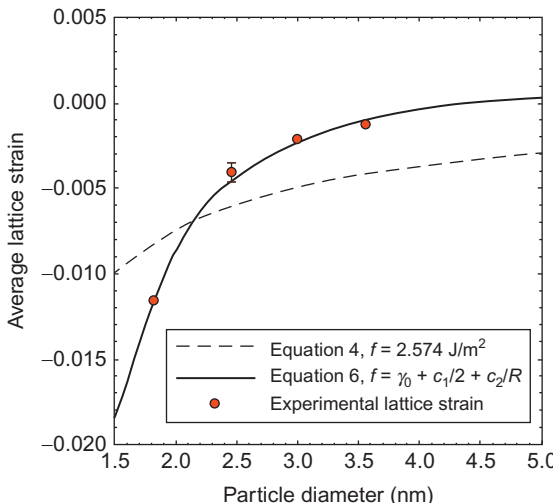


FIGURE 10.7 Plot of bond strain (defined in the text) versus nanoparticle size for Pt nanoparticles supported on carbon. The dashed line is the expected evolution of the bond strain due to surface tension effects given a size-independent bulk value for the surface energy. It clearly does not describe the observed behavior. The solid line is the result when a parameter is added that adds a term proportional to the curvature of the surface. This gives a very good fit (Redmond *et al.*, 2012).

we can extract this surface stress by fitting these strains. The result is shown in Fig. 10.7. The bond strain could not be explained with a size-independent surface stress, but adding an extra term that expressed the surface energy as a constant term, and a term proportional to the surface curvature, gave a good fit to the data.

10.2.6. Surface to Volume Ratio and Inhomogeneous Strains in Nanoparticles

The shift in the bond length shows the size-dependent average or homogeneous strain. If there is an inhomogeneous strain, such that some bonds are strained more than others, this will result in a broadening of the PDF peak. This might be expected as surface bonds, may be longer or shorter than bulk bonds. In a smaller nanoparticle, the surface bonds are a significant proportion of the total nanoparticle volume. If we define a surface annulus of thickness dr , the volume of the surface region is $4\pi r^2 dr$, and the interior volume of the particle is $(4/3)\pi r^3$ for a nanoparticle of diameter $d=2(r+dr)$. The surface to volume ratio is then

$$R = \frac{3dr}{r} = \frac{3dr}{d/2 - dr}. \quad (10.1)$$

If, for the sake of argument, we define the surface region to include all atoms that are within one nearest neighbor bond length of the surface (this is arguable but reasonable: all other atoms will be fully coordinated, though surface relaxations may extend deeper into the material), then $dr \sim 2 \text{ \AA}$ and $R = 3/(d/0.2 - 1)$ for d in nanometers. For 1.5, 2, 3, 4, 5, and 10 nm diameter NPs, this takes the values 0.46, 0.33, 0.21, 0.16, 0.125, and 0.06. What this means is that for tiny spherical 1.5-nm diameter nanoparticles, fully half of the atoms are surface atoms, and for a 2-nm diameter, one-third are. This drops off roughly as $1/d$, but already by 10 nm, only 6% of atoms are at the surface. Coming back to the inhomogeneous strain issue, if surface bonds have a different length than bulk bonds, we might expect a minority peak, or shoulder, to appear on the nearest neighbor bond peak in the PDF and for this to grow in intensity with decreasing NP size. In fact, as evident in Fig. 10.7, what appears to happen rather is that this peak gradually broadens with decreasing NP size, suggesting that bonds are relaxing somewhat throughout the nanoparticle to different degrees to accommodate the surface.

10.2.7. Size-Dependent Bond Stiffness in Nanoparticles

As well as bond strain, it would be nice to understand whether the bond stiffness is changing with NP size. Are the bonds getting weaker or stronger or staying the same strength in different sized nanoparticles? Information about bond stiffness can be extracted from the temperature dependence of the width of the PDF peaks. The width of the peaks consists of two components: vibrational amplitude and any static inhomogeneous strain, such as we have described above. It is a reasonably good assumption that the static strain distribution will not depend on temperature, and so by measuring the temperature dependence of the nanoparticle PDF peak widths, it is possible to separate these two components. This is generally done by fitting a Debye or Einstein model to the temperature dependence. This can be measured also using EXAFS and the existence of a NP size dependence of bond stiffness was shown to exist in quantum dot nanoparticles (Gilbert *et al.*, 2004a,b). For the nearest neighbor peak, PDF and EXAFS methods both give highly similar information in principle and no systematic study has been carried out to determine which is more accurate. In the case of the PDF, the temperature dependence of the width of higher neighbor peaks is also available allowing in principle a study to be carried out about the strength of different interactions in the material, such as bond stretch versus bond bending interactions as a function of NP size. In general, bond bending interactions are around $10 \times$ weaker than the stretching interactions in covalent semiconductors (Cai and Thorpe, 1992). In Fig. 10.8, we show fits of the Debye model (Debye, 1912; Billinge *et al.*, 1991) to the widths of the nearest neighbor PDF peak in different sized Pt nanoparticles as a function of temperature. For decreasing nanoparticle size, the curves become offset to higher values because of the size-dependent inhomogeneous strain described above. However, the

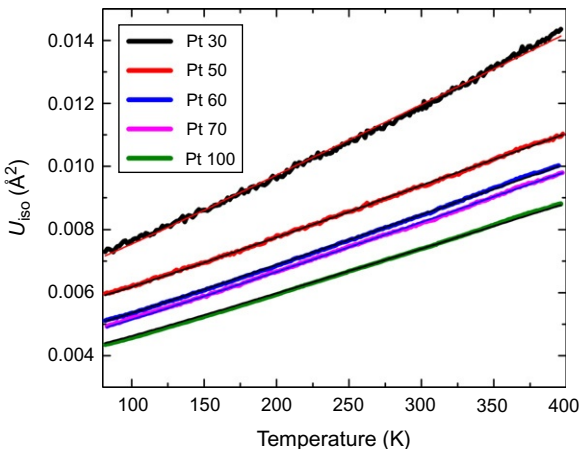


FIGURE 10.8 Temperature dependence of the width of the nearest neighbor Pt–Pt peak for nanoparticles of different sizes as follows: Pt 100, 70, 60, 50, and 30 have diameters 11.2, 3.7, 3.1, 2.5, and 1.8 Å, respectively. As the nanoparticles decrease in size, the curves become offset to higher values due to the increase in the static inhomogeneous strain with decreasing nanoparticle diameter. The fits of the temperature dependence to the Debye model also indicate that the bonding becomes softer with decreasing nanoparticle size, resulting in Debye temperatures of 252, 235, 226, 220, and 181 K, respectively (Shi *et al.*, 2012).

temperature-dependent slopes of the curves also increase slightly with decreasing NP size, confirmed by fits to a Debye model, which shows that the bonding in the nanoparticles is becoming softer with decreasing nanoparticle size.

10.2.8. Modeling Heterogeneous Nanoparticles

Everything that has been discussed thus far has been achieved by model-independent analysis or by fitting structural models that use a uniform bulk structure where the nanoparticle effects are taken into account by attenuating the PDF peak amplitudes with a characteristic function, which is the autocorrelation of the shape function of the particle, as discussed in Chapter 3. This is not expected to work well for heterogeneous nanoparticles such as core–shell nanoparticles that have a different material in the core surrounded by a second material. In this case, we need modeling approaches that can simulate the PDF from discrete objects. Taking this next step increases the complexity of the modeling process immensely. It is actually quite remarkable how much information can be obtained from the simple modeling approaches described above, and researchers should think carefully about diminishing returns before turning to approaches that model discrete nanoparticles where considerable effort may be expended for incremental (or in some cases no) increases in information about the material under study. For example, in the core–shell nanoparticle case described above, if the core and the shell structures do not have a definite

orientational relationship (i.e., if, when averaged over all the nanoparticles in the sample, there is no apparent epitaxy between the structure of the core and the shell), then even the core–shell nanoparticles can be successfully modeled in a two-nanoparticle-phase fit where the shape of one of the nanoparticle phases is spherical with the diameter of the core, and the shape of the other phase is a hollow spherical shell of the correct dimensions. This fitting is relatively quick. The only information that is left in the data about the epitaxial relationship between the core and the shell will be features in the difference curve that survive this approach. If, after this modeling is accomplished, there are no features other than incoherent noise ripples, further modeling may not be warranted. However, if there are still features in the difference curve, then powerful modeling approaches for discrete, heterogeneous, nanoparticles are now emerging for carrying out such an analysis. An explicit example of this is shown in Fig. 10.9. Here gold nanoparticles capped with $\text{CF}_3(\text{CF}_2)_5(\text{CH}_2)_2\text{SH}$ were measured and models are compared. The top panel shows the fit of an attenuated piece of bulk gold using PDFgui. There is a satisfactory fit, but features, especially in the low- r region, are clearly missed. The central panel shows a two-phase fit using PDFgui of the nanoparticle and the surface ligand material. Although it is not a correct physical model, because it neglects atomic pair correlations between the nanoparticle and the ligand, it results in an improved fit. In particular, the features in the low- r region are fit better. There are still some features in the residual curve, which may contain information about what is missing in this model: how the surface ligands attach to the nanoparticle. In the lower panel, the PDF from a model of a discrete nanoparticle built up using DISCUS (see below) is shown. The fit is worse, in part, because the model has not been refined (which requires a computationally expensive procedure discussed in Chapter 6 and which, at the time of writing, had not been published). This model seems to be taking the fit in the right direction (a feature at $\sim 3 \text{ \AA}$ is clearly coming from the NP–ligand–head bond), but many other inadequacies of the fit are not accounted for in the new model (e.g., the feature in the difference curve at around 5 \AA) and may not be accounted for in the refinement of this model when it is completed.

At the time of writing, the program that is most well developed for this is part of the DISCUS modeling package (Proffen and Neder, 1997; Korsunskiy *et al.*, 2007). It can directly simulate nanoparticles of different shape and size, including the presence of stacking faults (Kumpf *et al.*, 2005). Rather complex particle morphologies can be created, and there are good tools for one of the greatest challenges of this kind of modeling, the building of the complex nanoparticle models in the first place (Page *et al.*, 2010, 2011). Some interesting complex particle morphologies and their resulting PDFs are shown in Fig. 10.10. As described in Chapter 6 and below, the complex modeling framework program SrFit (Farrow *et al.*, 2012) can also calculate PDFs from discrete nanoparticle objects with different morphologies and carry out refinements on them, though at the time of writing is less developed than the

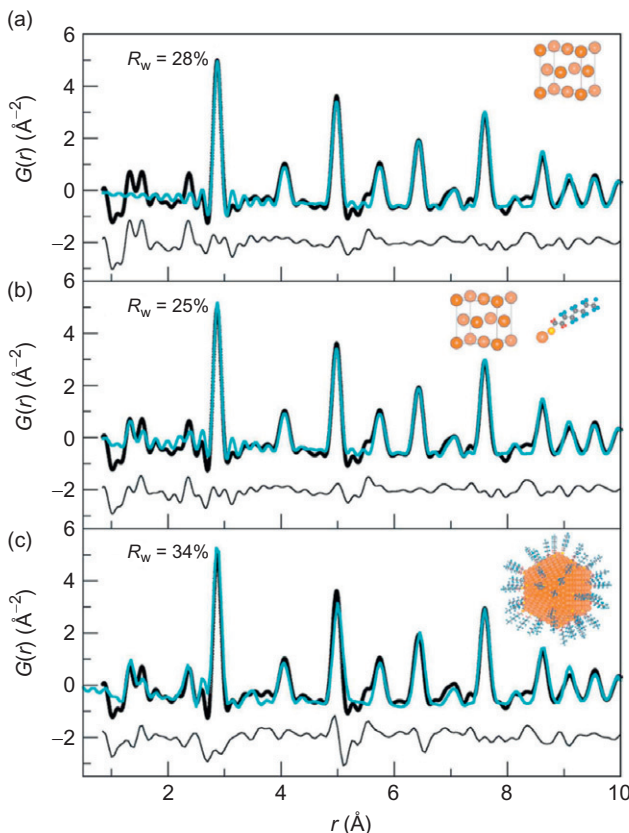


FIGURE 10.9 Measured PDFs (dark lines) and calculated PDFs (light lines) from gold nanoparticles capped with the surface ligand $\text{CF}_3(\text{CF}_2)_5(\text{CH}_2)_2\text{SH}$. (a) The fit using PDFgui for just the gold nanoparticle, ignoring any signal coming from the surface ligand. (b) Two-phase fit in PDFgui of the nanoparticle and the surface ligand material. The fit clearly improved. (c) Calculated PDF from a model of the nanoparticle with the surface ligands attached to the surface. This is not a best-fit model which may explain the worse agreement factor ([Page et al., 2011](#)).

capabilities of DISCUS. This kind of modeling is in its infancy and is certain to grow in the future.

10.2.9. Surface Capping Ligand Dependence of Nanoparticle Structure

Many nanoparticles are capped by organic ligands to stabilize them at their small sizes. Clearly, the ligands change the surface energy, bonding, electronic properties, etc. of the surface atoms, and should have an effect on the structure of the nanoparticles. This was shown in dramatic fashion in the case

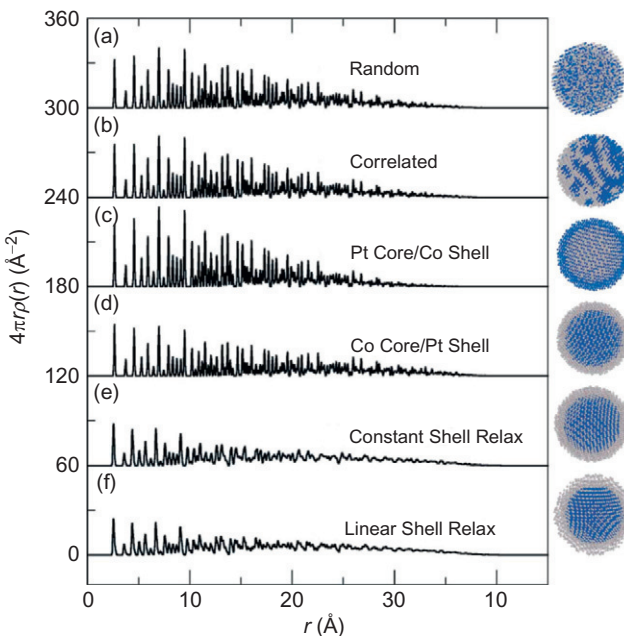


FIGURE 10.10 PDFs calculated from different complicated particle morphologies created using the program DISCUS (Page *et al.*, 2011).

of ZnS nanoparticles, where the internal structure of the nanoparticles was completely compromised by changing the hydration state of the surface capping ligands through drying (Zhang *et al.*, 2003; Gilbert *et al.*, 2004a,b). The effect on the PDF is shown rather dramatically in Fig. 10.11 (Gilbert *et al.*, 2004a,b). Such large effects are not always observed, however. In Fig. 10.12, we show the PDFs from very small (1.5 nm) sized CdSe nanoparticles (Cossairt *et al.*, 2011) where the surface capping ligand has been completely replaced. Though this change in the surface ligand significantly modifies the optical response of the particles, there is virtually no change in their internal atomic structure.

10.3. CLUSTERS SUSPENDED IN A SOLVENT

The PDF is ideal for studying clusters suspended in a liquid solvent for a number of reasons. First, the random orientations of the clusters result in the isotropic scattering ideal for PDF work. Second, the use of X-rays or neutrons as a probe results allows easy penetration of the liquid. Finally, the PDF measures instantaneous structure (Chapter 7) which means that it is not a problem that clusters may be dynamically tumbling in time. The main challenge in these experiments is the removal of the signal from the solvent,

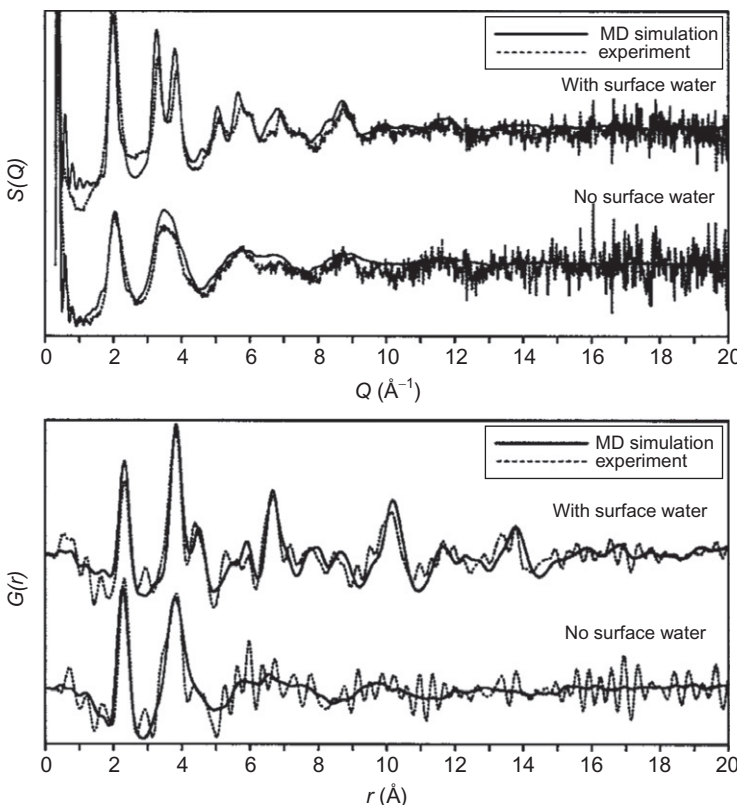


FIGURE 10.11 $S(Q)$ and $G(r)$ functions from ZnS nanoparticles where the data were collected from wet and dry nanoparticles, respectively. The size of the nanoparticles was 3 nm, but the size of the structural core is less, as evident from the loss of PDF peaks at high- r in the lower panel. A dramatic structural reorganization is observed on drying the nanoparticles (Gilbert *et al.*, 2004a,b).

though using modern sources and methods (e.g., the RAPDF approach) that give excellent statistics on the data (Chapter 4), and data modern processing methods (Chapter 5), rather high-quality data can be obtained.

10.3.1. Precursors to Gold Nanoparticle Formation

We mentioned above a study of gold nanoparticles suspended in water (Petkov *et al.*, 2005). In this case, the signal is strong, and there was no difficulty extracting the signal from the gold nanoparticles from the RAPDF X-ray data. If this can be extended to smaller solvated clusters that are actually in solution, then this approach can be used to study solvation of molecules and clusters, and to follow chemistry in real time. For example, it should be possible to study nanoparticle formation from dissolved precursors, chemical reactions in a hydrothermal environment, etc. This endeavor is at an early

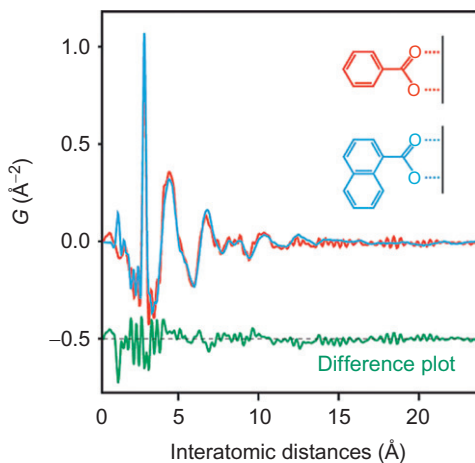


FIGURE 10.12 PDFs from ultra-small 1.5-nm CdSe nanoparticles made with two different capping ligands, benzoate (top) and 1-naphthoate (bottom). A difference curve between these two nanoparticle PDFs is shown below, and apart from noise, there is no difference at all (Cossairt *et al.*, 2011).

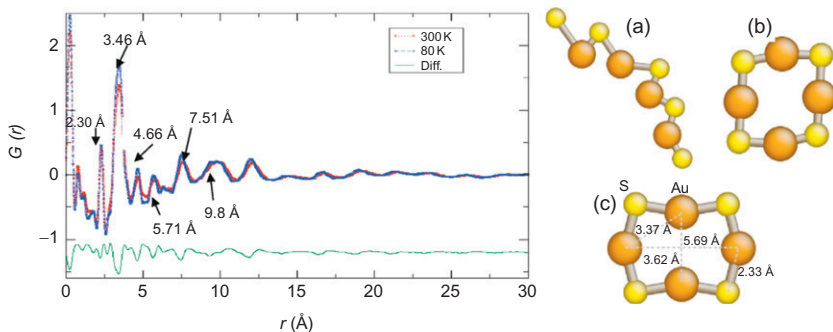


FIGURE 10.13 PDFs of dissolved precursor gold–sulfur species in water at two different temperatures, with a difference curve beneath (left). Different cluster models were fit to the data to determine the nature of the precursor cluster species in solution (right). The best agreement came from (C), the ring of four gold and four sulfur atoms where the sulfur makes a “staple” between neighboring gold atoms (Simpson *et al.*, 2010).

stage but looks highly promising. For example, the formation of gold nanoparticles from aqueous solution has been studied (Simpson *et al.*, 2010). The PDFs from the gold(I)–thiolate complexes in solution are shown in Fig. 10.13. It is clear that a strong PDF signal is obtained from the species in solution. Various structural models for the gold–thiolate complexes in solution were fit to the data, including chains, rings, and other structures. The most

successful was a ring of four gold and four sulfur ions where the sulfur makes “staples” pinning neighboring gold atoms that appear to survive in the surface capping ligands of the resulting gold nanoparticles ([Jadzinsky et al., 2007](#)). Thus, the thiol staples at the surface of the resulting nanoparticles are present in the solvated ligand complexes. Unfortunately, it was not possible to see intermediate clusters to follow the growth of the gold out of solution directly.

10.3.2. Time-Resolved Studies of Hydrothermal Chemical Reactions

In another similar application, hydrothermal synthesis of SnO_2 nanoparticles was studied from reagents in solution as a function of time in a reaction cell ([Jensen et al., 2012](#)). Hydrothermal synthesis shows greater promise for providing alternative pathways to reaction products at much lower temperatures and often milder conditions than other methods such as solid-state reaction. [Figure 10.14](#) shows a schematic of the *in situ* RAPDF apparatus. A great deal of detailed information was gained about the synthesis of SnO_2 nanoparticles by this route. For example, after being dissolved, tin(IV) forms clusters that are octahedrally coordinated by both Cl and water, forming aquachlorotin(IV) complexes of the form $[\text{SnCl}_x(\text{H}_2\text{O})_{6-x}]^{(4-x)+}$ as well as hexaaquat(in)IV complexes $[\text{Sn}(\text{H}_2\text{O})_{6-y}(\text{OH})y]^{(4-y)+}$. The existence of the two different complexes (with and without Cl) proved important for understanding the reaction. Upon heating, ellipsoidal nanoparticles of SnO_2 are formed but, crucially, only from the hexaaquat(in)IV clusters. Unexpectedly, the aquachlorotin(IV) do not react and their concentration in solution does not change with time during the synthesis. The resulting nanoparticle size and morphology depend on both the reaction temperature and the precursor concentration, as determined from quantitative modeling of the product nanoparticles. For example, the *c*-lattice parameter is expanded by up to 0.5% compared to the bulk for particle sizes down to

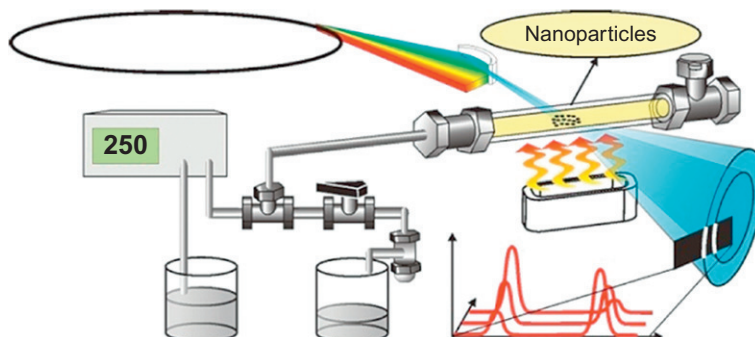


FIGURE 10.14 *In situ* setup for PDF experiments of hydrothermal synthesis ([Jensen et al., 2012](#)).

2–3 nm. SnO_2 nanoparticles below 3–4 nm do not form in the bulk rutile structure, but as an orthorhombic structural modification that previously had only been reported at high pressures above 5 GPa. From the time-dependent analysis, it could be shown that nanoparticle growth only takes place above 200 °C, and in general, the growth is limited by diffusion of precursor species to the growing particle (Jensen *et al.*, 2012). This kind of detailed information about the reaction mechanism is crucial for rational design of experiment protocols to obtain desired product properties. Some results of the work, including the time-dependent study, are summarized in Fig. 10.15. This shows the time dependence of the different reagents and products. Also shown are the PDFs obtained in the very short-time region of the synthesis where it was possible to see evidence for cluster aggregation, giving more information about the mechanism of cluster growth.

The data modeling made use of the new complex modeling program, SrFit (Farrow *et al.*, 2012), which turned out to be crucial. The reagents in the

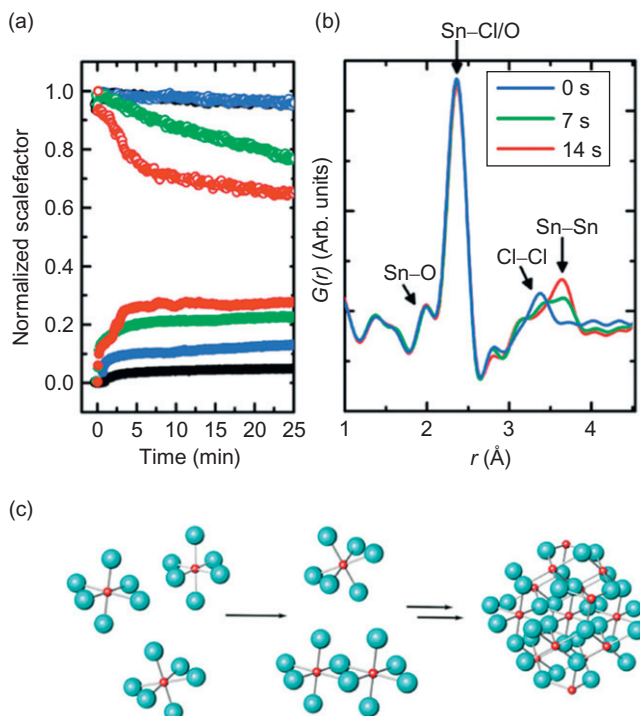


FIGURE 10.15 Results of the time-dependent PDF study of hydrothermal synthesis of SnO_2 nanoparticles (Jensen *et al.*, 2012). The PDF data (top right) were fit with models as a function of time during the synthesis. The top left panel shows refined normalized scale factors, which yield the concentrations of different reagents and products with time, for three different reaction conditions. The deduced reaction mechanism is shown at the bottom.

system were small, discrete octahedral clusters whereas the products were rather large nanoparticles. These two objects are best implemented in a modeling scenario in different representations. The clusters were modeled as discrete objects and the PDF was calculated using the Debye equation and then Fourier transformed to get the PDF. The SnO_2 nanoparticles were modeled in the same way as the CdSe nanoparticle studies described in [Section 10.2](#) as attenuated bulk material. This allowed very fast and efficient, yet accurate, refinements to be obtained over many datasets. SrFit is very flexible, even allowing models with different representations to be corefined to a single dataset.

10.3.3. Structures of Surfactant Micelles Suspended in Water

In something of a tour de force, a first ever atomic resolution structure study of micelles was recently demonstrated ([Hargreaves et al., 2011](#)). Micelles are very important in life and in technology. They are colloids of surfactant molecules suspended in water. The hydrophobic ends of the molecules cluster into balls away from the water that surrounds them, protected by hydrophilic head group. In this study, C_{10}TAB was studied. The TAB refers to alkyl-trimethylammonium bromide and C_{10} is a 10-atom alkyl carbon chain. This is the shortest carbon chain that actually forms micelles in suspension. It is an ionic surfactant with the Br^- going into solution, though presumably staying close to the micelle to maintain an overall charge neutrality, and the methylammonium becoming positively charged. It is widely used for things like templating silica to make other nanoporous materials, such as discussed in [Section 10.4](#), but micelles in general are also in paints, coatings, adhesives, cosmetics, oil recovery, and then remediating the environment by dispersing oil spills when they inevitably happen, and many also in many household products. They are also candidates for advanced drug delivery. Until this study, their structure had only been inferred indirectly from techniques such as SAS and light scattering (which indicate the overall size and shape of the particles), fluorescence and molecular spectroscopies, and electron paramagnetic resonance and nuclear magnetic resonance (NMR), for example ([Hargreaves et al., 2011](#)).

This structural study used empirical potential structure refinement (EPSR) modeling ([Section 6.3.3.1](#)) of multiple complementary datasets. In particular, samples with the same concentrations and chemistries, but with different levels of deuteration, were made up: five datasets were collected for 8 h each on fully deuterated CTAB in D_2O , H_2O , and a 50:50 $\text{D}_2\text{O}:\text{H}_2\text{O}$ mixture, on a sample of half:half deuterated and hydrogenated CTAB in H_2O and a hydrogenated CTAB sample in pure D_2O . The data were collected at the SANDALS instrument at ISIS. The resulting total scattering structure functions are shown in [Fig. 10.16](#). Notice how different the functions appear even though they are from nominally identical samples but collected with contrast

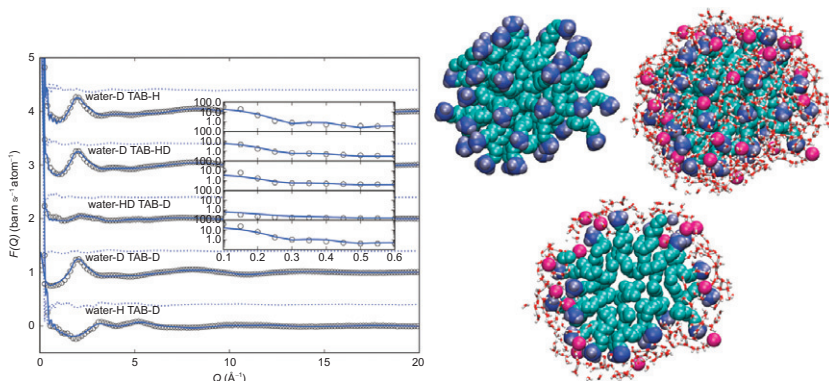


FIGURE 10.16 Five total scattering structure functions, including the low angle scattering (inset), from the surfactant micelles of CTAB collected with different hydrogen:deuterium substitutions (left). Representative structures of the resulting micelles obtained from the modeling (right). These are 43 surfactant micelles: just the surfactant molecules (top left), the micelle surrounded by bromide counterions and water molecules (top right), and the same micelle but in cross section of 12 \AA in width (bottom). (Hargreaves *et al.*, 2011).

agents on the atomic sites. If indeed the samples are identical (always a potential criticism of this approach), this gives multiple complementary datasets for the fitting. As described in Section 6.3.3.1, EPSR makes a Big Box of atoms (of order 10,000 in this case) but refines a small number of parameters that relate to the interatomic pair potentials between the molecules (the molecules are treated as rigid where their internal degrees of freedom are rigid). The data included the SAS region. Note that this kind of SAS:WAS (or as we describe in Section 4.3.2.1 perhaps it should be called MAS:WAS) study will become even more powerful with the recent commissioning of the NIMROD instrument at ISIS that measures both the small angle and wide angle scattering at the same time over a much wider Q -range.

The initial configurations of molecules and water were random, but in the modeling, the molecules quickly formed into micelles as shown in Fig. 10.16 on the right. The micelles are soft and the molecules flexible, so the micelle structures are statistical rather than absolute structure solutions with completely determined atomic positions, and the structures in the figure are representative of the micelles in the ensemble. The simulations are not quick (they ran for 200 days, more than half a year, on a cluster computer with around 800 cores), but they yield interesting information. The average micelle contained around 44 molecules in agreement with other indirect studies, with sizes ranging from 39 to 50 atoms (though it would be nice to have larger simulations and run them for longer to make sure that this is truly the equilibrium situation). The micelles were found to be almost spherical, again in agreement with indirect studies. The most important new information was atomic scale though. The Stern layer was

studied. This is the layer of bromide ions and hydrating water molecules that provide charge balance stabilize the micelles and allow them to pack more closely without repelling each other. It was found that there were 0.7 bromide ions and 21 water molecules per surfactant sitting just outside the surface of the micelle. The chemical composition of the average radial cross section was determined indicating how the molecules arrange in the micelles. Surprisingly, the interfacial shell between the micelle and the surrounding water was found to be very broad, 15 Å thick on average.

10.3.4. Structure of Pt(II) ion Complexes in Water

As discussed in section 10.2, Pt nanoparticles are of enormous importance in various applications, especially in catalysis. The nanoparticles are often formed from Pt(II) complexes in solution, and there is controversy about the precise nature of these solvated complexes (Bowron *et al.*, 2012). Pt(II) and Pd(II) ions form a stable planar tetramer with four water molecules lying around the cation to form an aqua ion. The main structural issues are what happens in the less tightly bound hydration layers, especially in the axial regions above and below the plane of the aqua ion, where species are thought to enter and leave during reactions (Marcus, 1986). The issue was controversial because the axial water ions were not found convincingly in EXAFS (Ayala *et al.*, 2001) or wide angle X-ray diffraction measurements (Hellquist *et al.*, 1991; Deeth and Elding, 1996), though they were seen in molecular dynamics simulations (Martinez *et al.*, 2004). However, a recent study of the Pd ion case using multiple datasets and EPSR modeling convincingly found the axial hydration shell (Bowron *et al.*, 2012). In this case, the datasets used were neutron total scattering measurements of the Pd ions in H₂O, D₂O, and a 1:1 D₂O:H₂O mixture and total scattering X-ray and EXAFS data of Pt in H₂O as shown in Fig. 10.17. The results of the fits clearly support the existence of a well-defined hydration shell in the axial direction, essentially resolving the controversy. In this study, the multiple isotope neutron data were complemented with X-ray and EXAFS data. The latter are dominated by the nearest neighbor hydration shell of the Pd which forms the aqua ion. The EXAFS pattern was simulated from the EPSR model and was in good agreement with the measured EXAFS, though in this case it appears to have added little information, other than being a reality check that the model is valid, as the Pd aqua ion was defined as a rigid molecule in the modeling. However, this EXAFS capability will in EPSR add more value in future studies. Nonetheless, the study found clear evidence for the axial hydration shell situated 2.85 Å above the Pd ion and containing, on average, two water molecules, with this shell being rather robust, surviving as it does in the acidic experiment conditions at high concentrations of ions (Bowron *et al.*, 2012).

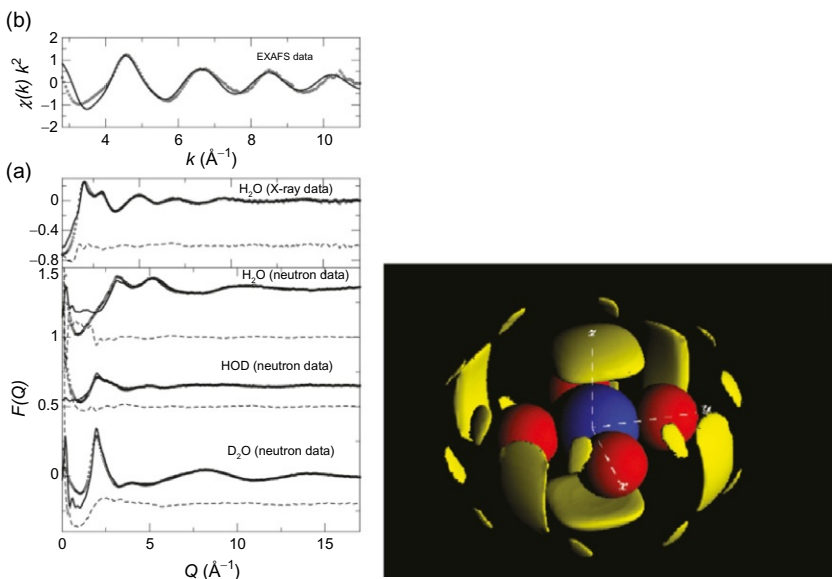


FIGURE 10.17 Independent neutron, X-ray (a), and EXAFS (b) datasets are shown as the dots. The EPSR model fits are shown as the solid lines and the difference curves as dashed curves (left). The resulting atomic isoprobability surfaces showing the arrangement of water around the Pt(II) ion (right). The Pt is the object at the center surrounded by four closely coordinate water molecules shown as spheres in a planar arrangement, the so-called Pt aqua ion. The outer, more diffuse, distributions of atomic density coming from water show the second hydration shell. There is clearly a well-defined water hydration shell in the axial position along z (Bowron *et al.*, 2012).

10.4. CLUSTERS AND MOLECULES INTERCALATED IN NANOPOROUS SOLIDS

10.4.1. Hydrogen in a Cyanide Host

An important use of nanoporous materials are as hosts for hydrogen as a fuel in mobile energy applications (e.g., see Zhao *et al.*, 2004). It is of the greatest importance to understand the H₂-host interactions in H₂-loaded nanoporous materials to aid efforts to increase hydrogen loading capacities and hydrogen exchange properties in new materials. One class of promising materials in this regard are nanoporous cyanide “Prussian Blue” compounds (Chapman *et al.*, 2005; Kaye and Long, 2005). Intercalated hydrogen is difficult to see because of its weak scattering in X-rays and incoherent scattering in neutron measurements. However, despite the difficulties, a PDF measurement that differentiated the loaded and unloaded cyanide host gave a clear H₂ signal even with X-rays, with the same model confirmed in a neutron measurement, as shown in Fig. 10.18 (Chapman *et al.*, 2006). The differences between the loaded and unloaded PDF signals are small but reproducible, convincingly allowing the

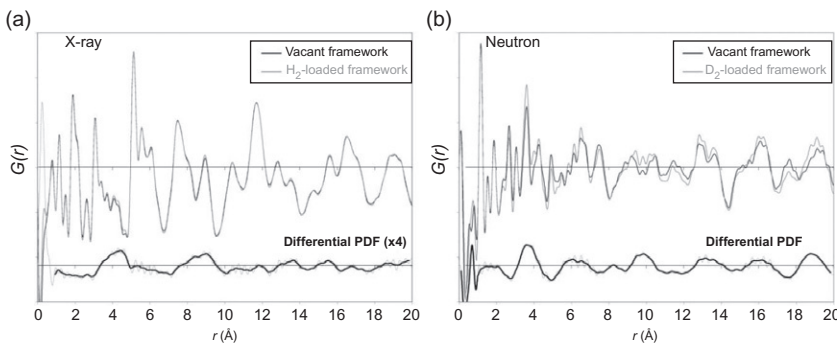


FIGURE 10.18 PDFs of Prussian Blue in the hydrogen loaded and unloaded condition (a). (left) RAPDF X-ray measurement (neutron diffraction measurement on a deuterated sample) (b). The difference between the loaded and the unloaded sample is shown offset below on an expanded scale (Chapman *et al.*, 2006).

H₂ molecules to be located in the structure. Contrary to expectation, it was shown that the hydrogen resides in a disordered arrangement around the centers of the pores and not bound to metal centers in the framework.

10.4.2. Metal Organic Frameworks and ZIFs

Metal organic frameworks (MOFs) are extremely interesting materials that are versatile and varied to make but have excellent properties, especially for valuable for their tunable porosity (Eddaoudi *et al.*, 2001; Kitagawa *et al.*, 2004; Rao *et al.*, 2008). They are formed by coordination chemistry of rigid units that form the vertices (with well-defined bond angles and coordinations) and the edges (with tunable length) that allow the creation of different structures of interconnected geometric hollow shapes. They have potential applications in all areas where nanoporous materials are used as molecular hosts, for example, hydrogen storage. They often form well-ordered crystals, in which case, the structures can be solved crystallographically, but also frequently they are not well ordered. A particular type of MOF that is susceptible to amorphization is zeolithic imidazolate frameworks (ZIFs) which have zinc imidazolate vertices and SiO₂ linkages. These materials were recently studied using total scattering (Bennett *et al.*, 2010). Neutron powder diffraction data were collected from perdeuterated (to remove the incoherent scattering from hydrogen) samples at the GEM diffractometer at ISIS, and X-ray total scattering data collected on an in-house diffractometer were modeled using RMC (Section 6.3.2). The ZIF was amorphized by heating. The existence of crystalline analog structures nearby gave a starting point to the study, and the PDFs of the amorphous and crystalline ZIFs were found to be highly similar in the low-*Q* region but differed in the region above 10 Å. The different ZIF structures and the RMC fits to the data are shown in Fig. 10.19. A key finding of the RMC modeling was that network modification was taking place as the samples amorphized with the topology of the network, as well as its

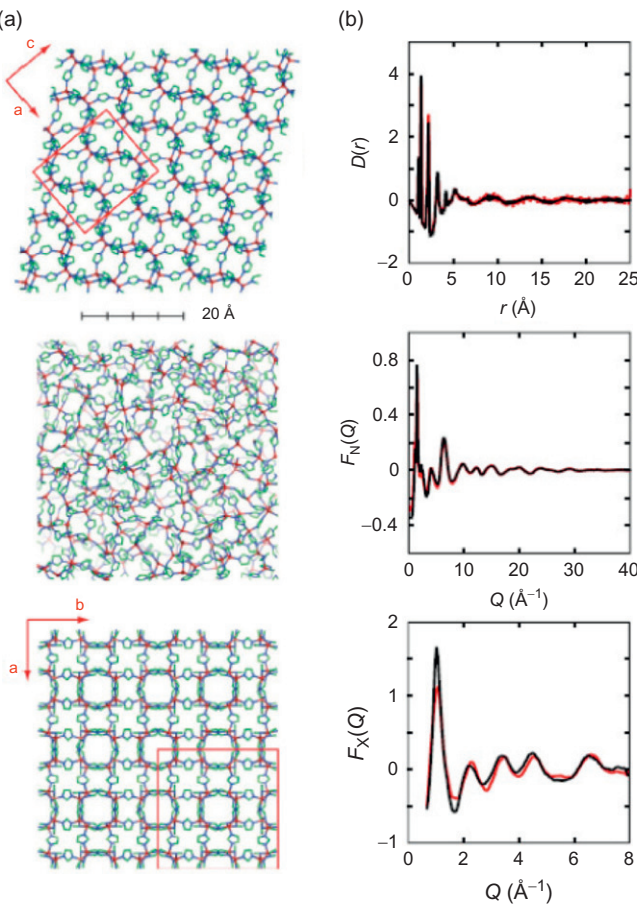


FIGURE 10.19 RMC study of neutron and X-ray total scattering data from amorphized ZIF compounds (Bennett *et al.*, 2010). On the left are three different ZIF structures, from top to bottom, ZIF-4, amorphous-ZIF, and ZIF-zni. On the right are the data from the amorphous sample (dark symbols) and the RMC fits (solid lines) to the PDF (top) and neutron and X-ray $F(Q)$ functions (Bennett *et al.*, 2010).

geometry, becoming randomized. The resulting network bore a striking resemblance to a continuous random network (CRN) more usually associated with silica glass, and in fact the RMC model of a-ZIF that was based on a silica CRN topology gave good agreement with both the neutron and X-ray total scattering data. The data were not sensitive enough to resolve subtleties about higher order ring statistics between the ZIF and silica CRN, which will require further study. The RMC study of this material gave clear insights into the structure and physics of these materials without any hint of data overinterpretation and is something of a model use of these methods to complex materials problems.

10.4.3. Mercury in Silica

Nanoporous silica is an important material for hosting chemical species. It is made by a templating method where soluble silica polymerizes around surfactant micelles. The most famous form was invented at Mobil Corporation and is called MCM-41 ([Beck et al., 1992](#)). This uses a charged surfactant which results in a template of ordered columnar micelles and the pores in the material are uniform, straight and ordered into a regular hexagonal array. An alternative approach, using charge neutral surfactants as the templates, results in a material where the pores are also uniform and elongated, but disordered in space and direction. The material resembles the Babinet couple of a plate of spaghetti. The pores of these materials can be functionalized, for example, by incorporating molecules containing sulfur ions such as mercaptan. They then become excellent molecular sponges that can be used for environmental remediation of troublesome heavy metal species such as mercury, in groundwater ([Billinge et al., 2005](#)). This material was studied using PDF methods as a function of mercury loading to determine the nature of the intercalated species after uptake of mercury. The resulting PDFs are shown in [Fig. 10.20](#). The unloaded silica host is on the bottom most PDF curve with its well-defined Si—O peak evident at 1.6 Å. There are five other PDF curves corresponding to different loadings of mercury. Multiple samples that used different silica hosts but had the same loading are plotted on top of each other. The PDFs have been rescaled so that their Si—O peaks have the same integrated area, that is, they are scaled per silica unit. It is immediately evident that new features, notably at 2.8 and 3.3 Å, grow up with increasing Hg loading. These features are presumably related to the Hg ions that have been taken up. An early EXAFS study ([Chen et al., 2004](#)) indicated that the loaded mercury had a significant number of oxygen neighbors, though the PDF data showed that this was not the case in the current samples: no correlations appeared in the PDF at the Hg—O bond length of 2 Å. Instead, the features in the PDF could be well explained as coming from zig-zag Hg—S chains existing in the pores of the material that resembled the Hg—S chains in the HgS mineral cinnabar. In cinnabar, the zig-zag chains stack into a well-ordered 3D array. In the nanoporous silica, they do not stack and presumably exist in the pores as individual zig-zag ropes. Although the species are not ordered and are embedded in a host species, the PDF gives important information about their structure and chemistry.

10.4.4. Sodium in Silica

The use of nanoporous silica has also been explored as a way of containing strong reducing agents such as alkali metals used in hydrogen production and chemical synthesis ([Dye et al., 2005](#)). These metals are pyrophoric and will spontaneously catch fire when they come into contact with water or moist air, making their transportation and storage quite hazardous. It was found that the

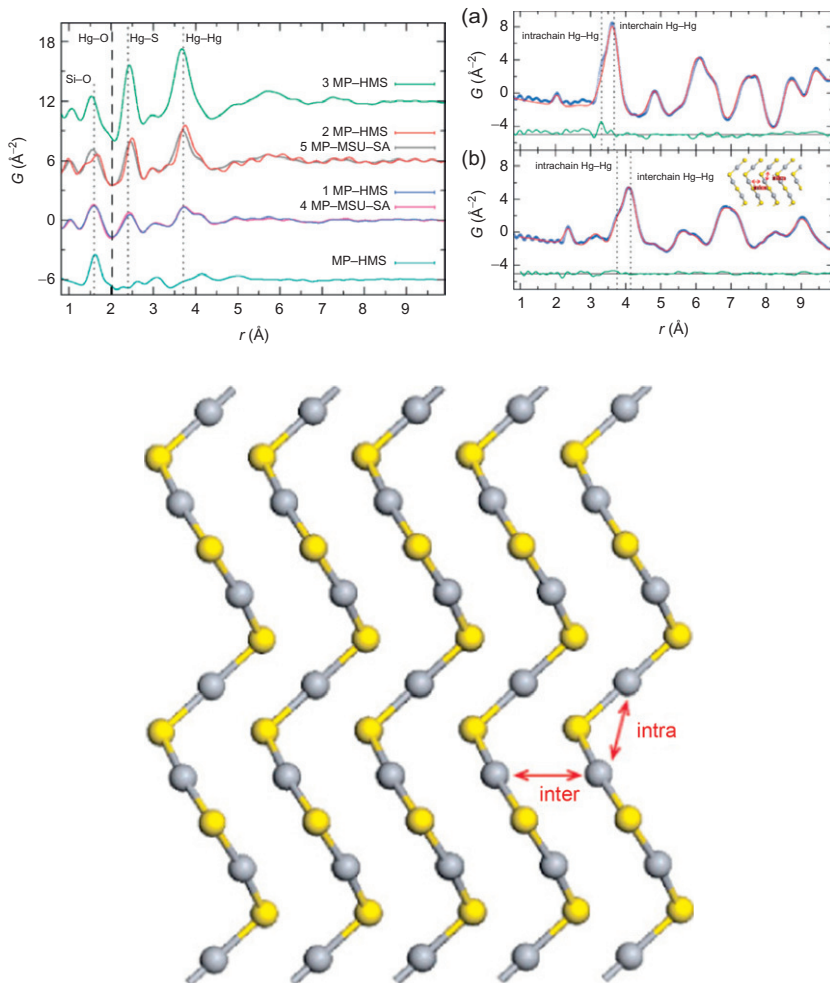


FIGURE 10.20 (Left) PDFs from mercury clusters intercalated into nanoporous silica. There are six curves from six different samples with four different mercury loading levels. The different samples with the same Hg loading are plotted on top of each other and the others are offset. The bottom curve is the nanoporous silica with no loading.

alkali metals can be incorporated into the nanoporous vycor silica glass (illustrated in Fig. 10.21), at up to 40 wt% retaining the same reducing power as the parent alkali metals but being stable in moist air and nonpyrophoric (Dye *et al.*, 2005). The material changed when it was subjected to modest temperature heat treatments in inert atmospheres, but the nature of the alkali metals after intercalation and the products after heat treatment were not known and were studied using PDF methods combined with NMR (Shatnawi *et al.*, 2007).

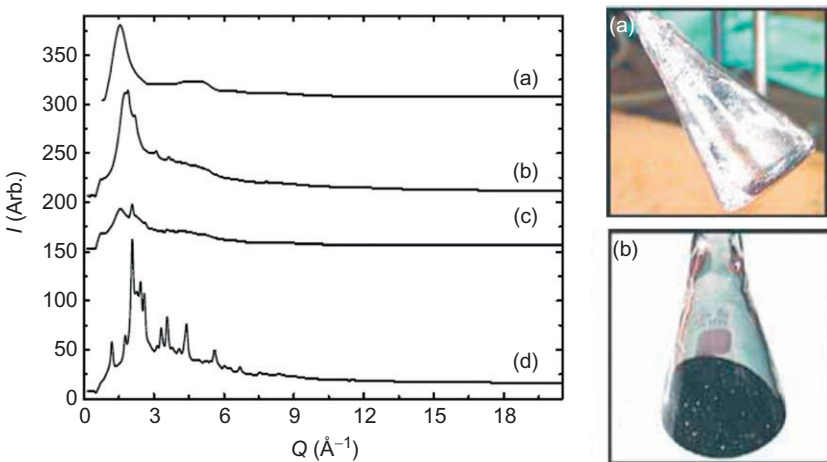


FIGURE 10.21 Diffraction patterns from silica and alkali metal-loaded silica. (a) Empty silica, (b) after Na loading (c), after low temperature heat treatment, and (d) after higher temperature heat treatment (left) (Shatnawi *et al.*, 2007). Photos of the liquid alkali metal mixed with nanoporous vycor silica before (top) and after (bottom) intercalation and heat treatment (right) (Dye *et al.*, 2005).

The experimental difficulties are evident in Fig. 10.21 which shows the diffraction patterns from the samples. The top curve is the amorphous silica host, then below it is the as-intercalated sample containing Na. The signal from the Na is hardly discernible. After heat treatment at 160 °C, some slightly clearer features are observed, and the material shows much more order after a 400 °C heat treatment on the bottom. In part because of a nice separation in r -space, the PDFs show much more information, as evident in Fig. 10.22. The PDF of amorphous silica ($\alpha\text{-SiO}_2$) dominates the PDF in the low- r region, but above around 10 Å, the PDF of $\alpha\text{-SiO}_2$ is flat. However, a residual signal is observed in this region in the loaded samples. A model of 4.8 nm diameter nanoparticles of b.c.c. sodium gives a good fit to the data in this region, though somewhat surprisingly a very large ADP is needed to fit the data. This implies that the Na in the pores is in the metallic state, though the NMR shows that there is a small proportion of Na^+ ions roughly consistent with them being a monolayer on the surface of the silica pores. This is consistent with the observation of ionized Na^+ in the much smaller pores of a zeolite (Petkov *et al.*, 2002) which formed what is thought to be a rare room temperature stable electrode material.

After heat treatment, the structure of the intercalated material changes, and the 400 °C treatment results in the sodium attacking and reacting with the silica host. A two-phase fit to the resulting PDFs indicated that the reaction products were sodium silicate, Na_2SiO_3 , and sodium silicide NaSi in precisely the right proportions if the chemical reaction was $5\text{Na} + 3\text{SiO}_2 \rightarrow 2\text{Na}_2\text{SiO}_3 + \text{NaSi}$. This

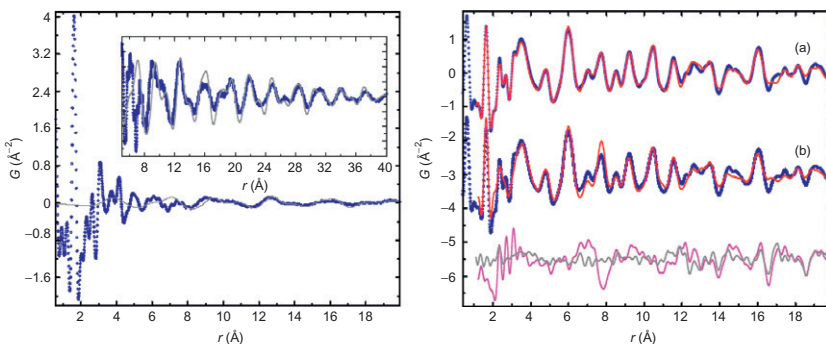


FIGURE 10.22 (Left) PDFs of sodium intercalated into nanoporous vycor silica. Symbols are the data. A strong signal from the silica is evident in the low- r region. In the high- r region where the PDF of silica is flat a residual signal persists. This is shown in the inset on expanded x - and y -scales. The PDF of b.c.c. sodium metal is shown as the solid line and agrees well with the data (right) PDFs of the same system after a 400 °C heat treatment. The data are the solid symbols. The top shows a fit to the data of a model (solid line) of sodium silicate. The lower curve shows a two-phase fit of sodium silicate and sodium silicide. Offset below are the difference curves showing the improved fit when the sodium silicide model is added ([Shatnawi et al., 2007](#)).

is a relatively low cost, low energy way to obtain the silicide, and the material has commercial applications. The PDF gave a very precise and quantitative picture of the structure of the intercalated material at each stage of the processing.

REFERENCES

- Ayala, R., Sanchez, M.E., Daz-Moreno, S., Sole, V.A. & Munoz, P.A. (2001) *J. Phys. Chem. B*, **105**, 7588.
- Bawendi, M.G., Kortan, A.R., Steigerwald, M.L. & Brus, L.E. (1989) *J. Chem. Phys.*, **91**, 7282.
- Beck, J.L., Vartuli, J.C., Roth, W.J., Leonowicz, M.E., Kresse, C.T., Schmitt, K.D., Chu, C.T.W., Olson, D.H., Sheppard, E.W., McCullen, S.B., Higgins, J.B. & Schlenker, J.L. (1992) *J. Am. Chem. Soc.*, **114**, 10834.
- Bennett, T.D., Goodwin, A.L., Dove, M.T., Keen, D.A., Tucker, M.G., Barney, E.R., Soper, A.K., Bithell, E.G., Tan, J.C. & Cheetham, A.K. (2010) *Phys. Rev. Lett.*, **104**, 115503.
- Billinge, S.J.L., Davies, P.K., Egami, T. & Catlow, C.R.A. (1991) *Phys. Rev. B*, **43**, 10340.
- Billinge, S.J.L., McKimmy, E.J., Shatnawi, M., Kim, H.J., Petkov, V., Wermeille, D. & Pinnavaia, T.J. (2005) *J. Am. Chem. Soc.*, **127**, 8492.
- Bowron, D.T., Beret, E.C., Martin-Zamora, E., Soper, A.K. & Marcos, E.S. (2012) *J. Am. Chem. Soc.*, **134**, 962.
- Bruchez, M., Moronne, M., Gin, P., Weiss, S. & Alivisatos, A.P. (1998) *Science*, **281**, 2013.
- Cai, Y. & Thorpe, M.F. (1992) *Phys. Rev. B*, **46**, 15879.
- Chapman, K.W., Southon, P.D., Weeks, C.L. & Kepert, C.J. (2005) *Chem. Commun.*, **26**, 3322.
- Chapman, K.W., Chupas, P.J., Maxey, E.R. & Richardson, J.W. (2006) *Chem. Commun.*, **38**, 4013.
- Chapman, H.N., Fromme, P., Barty, A., et al. (2011) *Nature*, **470**, 73.
- Chen, C.C., McKimmy, E.J., Pinnavaia, T.J. & Hayes, K.F. (2004) *Environ. Sci.*, **38**, 4758.
- Colvin, V.L., Schlamp, M.C. & Alivisatos, A.P. (1994) *Nature*, **370**, 354.

- Cossairt, B.M., Juhas, P., Billinge, S.J.L. & Owen, J.S. (2011) *J. Phys. Chem. Lett.*, **2**, 3075.
- Debye, P. (1912) *Ann. Phys.*, **39**, 789.
- Deeth, R.J. & Elding, L. (1996) *Inorg. Chem.*, **35**, 5019.
- Dmowski, W., Egami, T., Swider-Lyons, K.E., Love, C.T. & Rolison, D.R. (2002) *J. Phys. Chem. B*, **106**, 12677.
- Dmowski, W., Yin, H., Dai, S., Overbury, S.H. & Egami, T. (2010) *J. Chem. Phys. C*, **114**, 6983.
- Dye, J.L., Cram, K.D., Urbin, S.A., Redko, M.Y., Jackson, J.E. & Lefenfeld, M. (2005) *J. Am. Chem. Soc.*, **127**, 9338.
- Eddaoudi, M., Moler, D.B., Li, H.L., Chen, B.L., Reineke, T.M., O'Keeffe, M. & Yaghi, O.M. (2001) *Acc. Chem. Res.*, **34**, 319.
- Farrow, C.L. & Billinge, S.J.L. (2009) *Acta Crystallogr. A*, **65**, 232.
- Farrow, C.L., Juhas P., and Billinge S.J.L. 2012. (to be published).
- Gilbert, B., Huang, F., Zhang, H.Z., Waychunas, G.A. & Banfield, J.F. (2004a) *Science*, **305**, 651.
- Gilbert, B., Zhang, H.Z., Huang, F., Banfield, J.F., Ren, Y., Haskel, D., Lang, J.C., Srager, G., Jurgensen, A. & Waychunas, G.A. (2004b) *J. Chem. Phys.*, **120**, 11785.
- Guinier, A., Fournet, G., Walker, C. & Yudowitch, K. (1955) *Small-Angle Scattering of X-rays*. New York: John Wiley & Sons.
- Hargreaves, R., Bowron, D.T. & Edler, K. (2011) *J. Am. Chem. Soc.*, **133**, 16524.
- Haruta, M. (1997) *Catal. Today*, **36**, 15.
- Hellquist, B., Bengtsson, L., Holmberg, B., Hedman, B., Persson, I. & Elding, L.I. (1991) *Acta Chem. Scand.*, **45**, 449.
- Jadzinsky, P.D., Calero, G., Ackerson, C.J., Bushnell, D.A. & Komberg, R.D. (2007) *Science*, **318**, 430.
- Jensen, K.M., Christensen, M., Juhas, P., Tyrsted, C., Bojesen, E.D., Lock, N., Billinge, S.J.L. & Iversen, B.B. (2012) *J. Am. Chem. Soc.*, **134**, 6785.
- Juhas, P., Cherba, D.M., Duxbury, P.M., Punch, W.F. & Billinge, S.J.L. (2006) *Nature*, **440**, 655.
- Juhas, P., Granlund, L., Duxbury, P.M., Punch, W.F. & Billinge, S.J.L. (2008) *Acta Crystallogr. A*, **64**, 631.
- Kaye, S.S. & Long, J.R. (2005) *J. Am. Chem. Soc.*, **127**, 6506.
- Kitagawa, S., Kitaura, R. & Noro, S. (2004) *Angew. Chem. Int. Ed.*, **43**, 2334.
- Knecht, M.R., Weir, M.G., Myers, V.S., Pyrz, W.D., Ye, H.C., Petkov, V., Buttrey, D.J., Frenkel, A.I. & Crooks, R.M. (2008) *Chem. Mater.*, **20**, 5218.
- Kodama, K., Iikubo, S., Taguchi, T. & Shamoto, S. (2006) *Acta Crystallogr. A*, **62**, 444.
- Korsunskiy, V.I., Neder, R.B., Hofmann, A., Dembski, S., Graf, C. & Rühl, E. (2007) *J. Appl. Crystallogr.*, **40**, 975.
- Kumpf, C., Neder, R.B., Niederdraenk, F., Luczak, P., Stahl, A., Scheuermann, M., Joshi, S., Kulkarni, S.K., Barglik-Chory, C., Heske, C. & Umbach, E. (2005) *J. Chem. Phys.*, **123**, 224707.
- Li, L.S. & Alivisatos, A.P. (2003) *Phys. Rev. Lett.*, **90**, 097402.
- Marcus, Y. (1986) *Ion Solvation*. Chichester: John Wiley & Sons.
- Martinez, J.M., Torrico, F., Pappalardo, R.R. & Sanchez, M. (2004) *J. Phys. Chem. B*, **108**, 15851.
- Masadeh, A.S., Bozin, E.S., Farrow, C.L., Paglia, G., Juhás, P., Karkamkar, A., Kanatzidis, M.G. & Billinge, S.J.L. (2007) *Phys. Rev. B*, **76**, 115413.
- McKeown, D.A., Hagans, P.L., Carette, L.P.L., Russell, A.E., Swider, K.E. & Rolison, D.R. (1999) *J. Phys. Chem. B*, **103**, 4825.
- Murray, C.B., Kagan, C.R. & Bawendi, M.G. (1995) *Science*, **270**, 1335.
- Neder, R.B. & Proffen, T. (2009) *Diffuse Scattering and Defect Structure Simulations: A Cook Book Using the Program DISCUS*. Oxford: International Union of Crystallography, Oxford University Press.
- Page, K., Proffen, T., Terrones, H., Terrones, M., Yang, Y., Stemmer, S., Seshadri, R. & Cheetham, A.K. (2004) *Chem. Phys. Lett.*, **393**, 385.

- Page, K., Proffen, T., Niederberger, M. & Seshadri, R. (2010) *Chem. Mater.*, **22**, 4386.
- Page, K., Hood, T.C., Proffen, T. & Neder, R.B. (2011) *J. Appl. Crystallogr.*, **44**, 327.
- Petkov, V., DiFrancesco, R.G., Billinge, S.J.L., Acharya, M. & Foley, H.C. (1999) *Philos. Magn. B*, **79**, 1519.
- Petkov, V., Billinge, S.J.L., Vogt, T., Ichimura, S. & Dye, J.L. (2002) *Phys. Rev. Lett.*, **89**, 075502.
- Petkov, V., Peng, Y., Williams, G., Huang, B.H., Tomalia, D. & Ren, Y. (2005) *Phys. Rev. B*, **72**, 195402.
- Petkov, V., Gateski, M., Niederberger, M. & Ren, Y. (2006) *Chem. Mater.*, **18**, 814.
- Proffen, T. & Neder, R.B. (1997) *J. Appl. Cyrstallogr.*, **30**, 171.
- Rao, C.N.R., Cheetham, A.D. & Thirumurugan, A. (2008) *J. Phys. Condens. Mat.*, **20**, 083202.
- Redmond, E.L., Setzler, B.P., Mazaheripour, A., Juhas, P., Billinge, S.J.L., and Fuller T.F. 2012. (to be published).
- Scott, M.C., Chen, C.C., Mecklenburg, M., Zhu, C., Xu, R., Ercius, P., Dahmen, U., Regan, B.C. & Miao, J.W. (2012) *Nature*, **483**, 444.
- Seibert, M.M., Ekeberg, T.Maia, F.R.N.C., et al. (2011) *Nature*, **470**, 78.
- Shatnavi, M., Paglia, G., Dye, J.L., Cram, K.D., Lefenfeld, M. & Billinge, S.J.L. (2007) *J. Am. Chem. Soc.*, **129**, 1386.
- Shi, C., Redmond, E.L., Setzler, B.P., Mazaheripour, A., Juhas, P., Fuller, T.F., and Billinge S.J.L. 2012. (submitted for publication).
- Simpson, C.A., Farrow, C.L., Tian, P., Billinge, S.J.L., Huffman, B.J., Harkness, K.M. & Cliffel, D.E. (2010) *Inorg. Chem.*, **49**, 10858.
- Tolbert, S.H. & Alivisatos, P.A. (1994) *Science*, **265**, 373.
- Zhang, H.Z., Gilbert, B., Huang, F. & Banfield, J.F. (2003) *Nature*, **424**, 1025.
- Zhao, X.B., Xiao, B., Fletcher, A.J., Thomas, K.M., Bradshaw, D. & Rosseinsky, M.J. (2004) *Science*, **306**, 1012.
- Zuo, J.M., Vartanyants, I., Gao, M., Zhang, R. & Nagahara, L.A. (2003) *Science*, **300**, 1419.